Construction of Ce-MOF@COF hybrid nanostructure with controllable thickness for the electrochemical sensitive detection of metol
Peer-reviewed author version

Construction of Ce-MOF@COF hybrid nanostructure with controllable thickness for the electrochemical sensitive detection of metol

Xiaoxian Hu,[a] Jing Qian,[a] Juan Yang,[a,]* Xiaomin Hu,[a]

Yanjiao Zou,[a] Nianjun Yang[b,c]*

[a] School of Chemistry and Environmental Engineering, Key Laboratory of Green Chemical Engineering Process of Ministry of Education, Hubei Key Lab of Novel Reactor and Green Chemical Technology, Wuhan Institute of Technology, Wuhan 430073, China

[b] Department of Chemistry, Hasselt University, 3590 Diepenbeek, Belgium

[c] IMO-IMOMEC, Hasselt University, 3590 Diepenbeek, Belgium

* Corresponding Author;

E-mail addresses: jyangchem@wit.edu.cn; nianjun.yang@uhasselt.be

ABSTRACT

Covalent organic frameworks (COFs), a newly emerging kind of porous material, have gained extensive attention due to their fascinating structural features. However, the superiority of COFs as electrochemical sensing materials has not yet been adequately explored. Herein, a new type of core-shell metal-organic framework (MOF)@COF composites are synthesized through in situ growth of TAPB-DMTP-COF on the pre-synthesized Ce-BDC core. The thickness of the COF shell can be controlled to 20—50 nm by adjusting the Ce-MOF mass. It is found that the obtained MOF@COF composite possesses a larger electrochemical active area and faster electron transfer kinetic than its single component. As a case application of this composite, it has been employed as a sensing material for voltammetric detection of metol, where a linear range from 0.1 - 200 μM and a detection limit of 30 nM have been obtained. This study provides a new strategy to synthesize COF-based electrode materials as well as to explore their electrochemical properties and applications.

Keywords: Covalent organic framework, metal-organic framework, Nanostructure, Electrochemical sensors, Metol

1. Introduction

Covalent organic framework (COF) is a new class of crystalline porous organic network polymers. It has a predictable structure, which is formed from its organic building units *via* their strong covalent bonds [1-5]. Generally, COFs can be composed of light elements (e.g., B, C, N, O, Si) [6]. Since the innovative work was announced in 2005 by Yaghi and co-workers [7], the COFs have been studied in various fields, such as gas adsorption and separation [8-10], heterogeneous catalysis [11], energy storage (e.g. supercapacitors) [12, 13], chemical sensing, and drug delivery [14-16]. The driving force behind this is that the COFs feature many unique properties, such as low densities, ordered pore structures, high specific surface areas, good thermal/chemical stability, and tunable functions. In more detail, compared with other traditional crystalline porous polymers, the customizable pore sizes and functional groups of the COFs are efficient to bond with other guest molecules [17]. The interlayer overlapped π-π electron clouds and the π-conjugations within the layers of the COFs can accelerate charge transport along the self-assembled molecular columns [18, 19]. The chemical and thermal stability of the COFs is high. In addition to COF, metal organic framework (MOF) has been extensively investigated. It is a new and porous material, where organic ligands are linked with metal ions or metal clusters [20-22]. Similar to the COFs, the MOFs have been already employed in various application fields. For example, MOFs have emerged as a new type of electrocatalysts as well as electrode materials for various electrochemical sensing [23, 24]. Considering the intrinsic porosities of both MOFs and COFs, their integrations or their composites are expected to produce new materials that can own both inheritance of their porosities and the active centers of metal ions.

Recently, the synthesis and application of MOF/COF composites have attracted attention, especially in the fields of photocatalysis [25, 26] and gas separation [27, 28]. For example, Fu et al.[29] synthesized a novel class of COF@MOF composite membranes for H_2/CO_2 gas separation in 2016, which was considered to be one of the best separation membranes reported so far. In addition, the practicability of MOF/COF hybrid materials as sensing materials has also been explored. Zhang et al. [30] synthesized a core-shell MOF@COF hybrid using UiO-66- NH_2 as the core and TAPB-DMTP-COF (TAPB: 1,3,5-tris(4-aminophenyl) benzene; DMTP: 2,5-dimethoxy-p-phenylenedial) as the shell, and further use it for sensitive detection of

adenosine triphosphate (ATP) and chloramphenicol (CAP). Liu et al. [31] prepared a novel nanostructured Co-MOF-on-TPN-COF (TPN-COF: terephthalonitrile-based covalent organic framework) for constructing an ultrasensitive biological platform to monitor ampicillin. The detection limit of this sensor was low to 0.217 fg mL^{-1}. Zhou et al. [32] constructed a Ce-MOF@COF hybrid nanostructure as a label-free aptamer sensor. Although there have been some reports about the MOF/COF hybrid nanostructures, the variety of them is limited, and their application in the field of electrochemical sensing is still in its infancy.

Herein, a core-shell composite is designed using a Ce-MOF as the core and a TAPB-DMTP-COF as the shell. This MOF@COF composite thus has rich functional groups, a high surface area, and promoted electron transfer rates of electroactive species, endowing its electrochemical properties and applications.

In other words, the pairing MOFs and COFs, namely the interlayer overlapped π-π electron clouds and the π-conjugations might accelerate charge/electron transport of electroactive species in solutions. It has been shown that the covalent bonds between MOFs and COFs actually act as the "bridge" for electron transport [33, 34]. Meanwhile, the porosities of both COFs and MOFs increase the active surface areas of such hybrids. Consequently, the composites of COFs and MOFs are superior electrode materials over individual COFs or MOFs.

Metol (N-methyl-p-aminophenol sulphate), an environmental pollutant, is a common phenol chemical raw material commonly used to manufacture photographic developer. In recent years, the extensive use and discharge of developers have posed a certain threat to the water environment. More importantly, metol is difficult to be naturally degraded. Therefore, it is very important to establish a simple and accurate analytical method for the detection of metol. Some technologies such as photolysis [35], chromatography-mass spectrometry [36], advanced oxidation processes [37], and electrochemical analysis have been reported to determine the concentration of metol in a water environment. Unfortunately, some of these methods are time-consuming, poorly accurate, and have high instrument costs. Among them, the electrochemical method is widely used because of its high accuracy, simplicity, and rapid determination.

Thus, in this report, we report on the synthesis and characterization as well as electrochemical properties and applications of such a core-shell MOF@COF

composite. As a case study, its electrochemical sensing applications toward voltammetric detection of metol were detailed.

2. Experimental section

2.1. Reagents and materials

The chemicals of 2,5-dimethoxyterephaldehyde (DMTP, 97%), 1,4-benzenedicarboxylic acid (H$_2$BDC), and N, N-dimethylformamide (DMF) were purchased from Bidepharm Medical Technology Co., Ltd. (Shanghai, China); 1,3,5-tris(4-aminophenyl) benzene (TAPB, 97%), metol, bisphenol A (BPA), hydroquinone (HQ), catechol (CC), resorcinol (RC), 2,4-Dichlorophenol (2,4-DCP) was purchased from Aladdin Industrial Corporation (Shanghai, China); cerium ammonium nitrate ($(NH_4)_2Ce(NO_3)_6$), 1,4-dioxane, butanol, methanol, acetic acid, tetrahydrofuran, and acetone were purchased from Sinopharm Chemical Reagent Co., Ltd. (Shanghai, China). Triclosan (TCS) was purchased from Yuanye Bio-Technology Co., Ltd. (Shanghai, China). The phosphate-buffered solutions (PBS, 0.10M, pH 5.0 − 9.0) were prepared by using Na$_2$HPO$_4$ and NaH$_2$PO$_4$. All the solutions were prepared using ultrapure water obtained from a Milli-Q water purification system (Millipore, Bedford, MA, USA).

2.2. Instrumentation

The morphologies of as-synthesized nanomaterials were investigated using a Gemin-300 scanning electron microscope. A JEM-2100 microscope (JEOL Ltd., Tokyo, Japan) was applied to record their transmission electron microscopy (TEM) images. X-ray powder diffraction (XRD) data were collected using a Bruker D8 Advanced with DaVinci design instrument. An AXIS-UL TRA DLD-600W (SHIMADZU-Kratos Company, Japan) was used to investigate the elemental composition of the used samples. Their Raman spectra were collected on a Thermo Fischer DXR Raman spectroscopy with a 532 nm diode laser (Thermo Fisher Scientific, USA). Electrochemical experiments were performed on a CHI620E electrochemical workstation (Chenhua Instrument, Shanghai, China) with a three-electrode system. The reference and counter electrodes were a saturated calomel reference electrode (SCE) and a platinum wire, respectively. The working electrode was either a bare glassy carbon electrode (GCE, 3.0 mm in diameter) or a GCE coated with the Ce-

BDC MOF@COF composite. Before electrochemical measurements, the GCE was polished to a mirror-like surface with alumina slurry and then rinsed with ethanol and double-deionized water by sonication. To fabricate a GCE-modified electrode, 5.0 μL of Ce-BDC MOF or Ce-BDC MOF@COF was dropped on the surface of a clean GCE and further dried in air.

2.3. Materials synthesis

Synthesis of Ce-BDC MOF   Ce-based MOF was synthesized by solvothermal method [38]. In the first step, 35.4 mg of H_2BDC was dissolved in a mixture of DMF and formic acid (3 mL, v/v = 4:1) at room temperature. Subsequently, 1 mL of 0.3 M cerium ammonium nitrate $((NH_4)_2Ce(NO_3)_6)$ aqueous solution was drop-wisely injected into the above mixture. The resultant solution was homogeneous and sealed in a vial. After the reaction under static conditions at 60 °C for 2 h, the precipitates were centrifuged and washed with DMF and acetone for several times. Finally, the yellow product (Ce-BDC MOF) was dried at 60 °C in the air for 12 h. For the fabrication of modified electrodes, 2.0 mg Ce-BDC MOF was suspended in 1.0 mL ethanol and sonicated for 30 min until it became a homogeneous solution.

Synthesis of Ce-BDC@TAPB-DMTP-COF   The TAPB-DMTP-COF was synthesized according to a previously reported method [39]. Briefly, 0.0105 g of TAPB (0.030 mmol) and Ce-BDC MOF with a varied amount (e.g., 10, 20, 30, 40 mg) were added to 4.5 mL of 1,4-dioxane-butanol methanol (v/v/v = 4:4:1). This mixture was sonicated for 20 min till a homogenous solution was obtained, where 2,5-dimethoxyterephaldehyde (DMTP) (0.045 mmol, 0.0087 g) was then added. This mixture was further sonicated for 10 min till a homogenous solution was obtained. Subsequently, 0.050 mL of 12 M aqueous acetic acid was drop-wisely added. After the mixture was left undisturbed at room temperature for 2 h, it was heated at 70 °C for 24 h in an oven. Finally, the product was cooled down to room temperature. The resultant TAPB-DMTP-COF was washed several times with tetrahydrofuran and acetone before it was dried in a vacuum at room temperature for 12 h. As a control experiment, a bulk COF was synthesized using the same procedure except in the absence of Ce-BDC MOF. For the fabrication of modified electrodes, 2.0 mg Ce-BDC MOF was suspended in 1.0 mL ethanol and sonicated for 30 min until it became a

homogeneous solution.

2.4. Sample preparation

The supermarket receipt was obtained from the local campus supermarket (Wuhan, Hubei). 1 g of receipt was cut into pieces and then placed in 10 ml of anhydrous ethanol for 1 h with ultrasound assistance. After that, the filtrate was collected.

Lake water samples were obtained from local Jingsi Lake (Wuhan, Hubei). The lake water was filtered with a 0.22 µm filter membrane to remove impurities. The resulting filtrate was collected as an actual water sample.

3. Results and discussion

3.1. Characterization of Ce-BDC@COF composites

The morphology, size, and microstructures of Ce-BDC MOF, TAPB-DMTP-COF, and the Ce-BDC@COF composite were then examined using SEM and TEM. In the SEM (**Figure 1a**) and TEM (**Figure 1b**) images of Ce-BDC MOF, one can see that Ce-BDC MOF displays a well-defined octahedral shape with a smooth surface. Its average size is ca. 30 nm. Differently, TAPB-DMTP-COF is in the form of microspheres (**Figure 1c**) and their average size is ca. 150 nm (**Figure 1d**). In between them, there are abundant pores. For the Ce-BDC@COF composite, its surface is uniformly covered with a layer (**Figure 1e**). The particle size is about 100 nm (**Figure 1f**). Further comparison of their SEM and TEM (**Figure S1**), one can conclude that the Ce-BDC@COF composite consists of the Ce-BDC MOF polyhedral nanocrystals as the core, which was evenly covered by a shell layer of COF. The shell thickness is only about 22 - 70 nm. Moreover, the thickness of this COF film decreases when the amount of added MOF is increased. Consequently, the Ce-BDC@COF composite is formed with a perfect core-shell morphology.
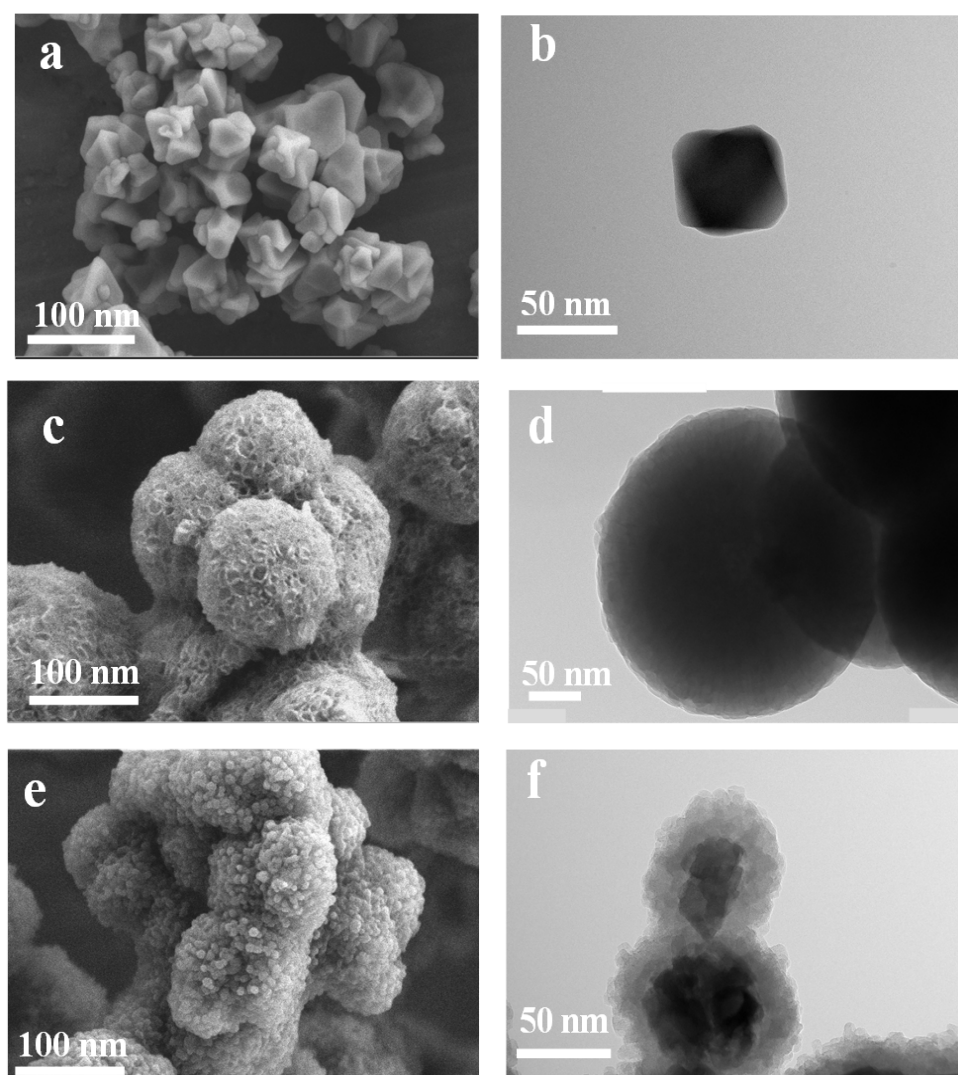
Figure 1. SEM and TEM images of Ce-BDC MOF (a,b), TAPB-DMTP-COF (c,d), and the Ce-BDC@COF composite with an amount of 20 mg Ce-BDC MOF (e,f).

The chemical composition and crystal structures of TAPB-DMTP-COF, Ce-BDC MOF, and the Ce-BDC@COF composites with different proportions of TAPB-DMTP-COF and Ce-BDC MOF were investigated by means of XRD. In their XRD patterns (**Figure 2**), the simulated peak positions of the pure TAPB-DMTP-COF [11] match well with the experimental ones. Six diffraction peaks at 2.79, 4.84, 5.60, 7.39, 9.73, and 25.42° are corresponded to the (100), (110), (200), (210), (220), and (001) planes, respectively. Meanwhile, the XRD patterns of Ce-BDC MOF match well with those in the literature [40]. The product is supposed to be composed of the $[Ce_6O_4(OH)_4]^{12+}$ clusters in the structural formula of $[Ce_6O_4(OH)_4(BDC)_6]$. These results confirm the successful synthesis of the Ce-BDC MOF. Furthermore, the peaks

of the Ce-BDC@COF composites are similar to those of pure Ce-BDC MOF, indicating the encapsulation of Ce-BDC MOF with TAPB-DMTP-COF does not change the crystalline structure of Ce-BDC MOF. Note that the positions of the main characteristic peaks of Ce-BDC MOF (at 7.14°) and TAPB-DMTP-COF (at 7.39°) are too close, the main peaks of Ce-BDC MOF and TAPB-DMTP-COF components in their composites are merged together. In the enlarged XRD patterns of the Ce-BDC@COF composites, the peaks at small angles appear as two characteristic peaks of the Ce-BDC MOF and the (210) crystal plane of TAPB-DMTP-COF (**Figure S2**). These results indicate that TAPB-DMTP-COF is successfully coated on the Ce-BDC MOF matrix. An increase in the Ce-BDC MOF content does not change the diffraction peaks of these composites, indicating that the two components retain their complete structures and crystallinity even after being covalently connected.
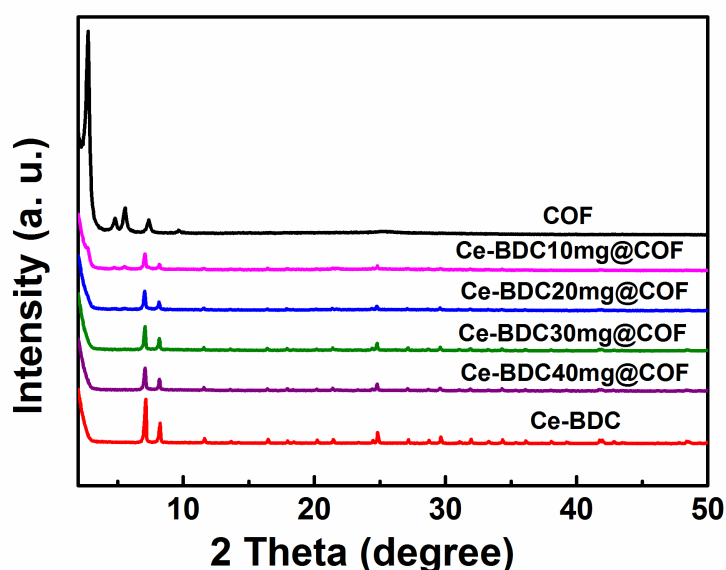

Figure 2. XRD patterns of TAPB-DMTP-COF, Ce-BDC MOF, and their composites (Ce-BDC@COFs) with different proportions.

The FTIR spectra of TAPB-DMTP-COF, Ce-BDC MOF, and Ce-BDC@COF composites were measured (**Figure 3**). In the spectrum of Ce-BDC MOF, the stretching vibration peaks of the –COO⁻ group appear at 1567 and 1384 cm⁻¹. In the spectrum of TAPB-DMTP-COF, the peaks at 1574 and 1268 cm⁻¹ belong to the groups of C=C and C–N, respectively. All these peaks are presented in the spectra of Ce-BDC@COF composites with different proportions of TAPB-DMTP-COF and Ce-

BDC MOF (**Figure S3**), again demonstrating the successful synthesis of the Ce-BDC@COF composites by use of the Schiff base reaction. Moreover, the bands at ca. 3330 and 1504 cm^{-1} are attributed to the coordinated H_2O molecules and the stretching vibrations of para-aromatic CH groups, respectively [41, 42]. The coordination interaction between Ce ions and the carboxylic acid group of H_2BDC can be evidenced by the shift of C=O stretching frequency from 1715 to 1660 cm^{-1} for the uncoordinated organic ligand - H_2BDC [43-44].
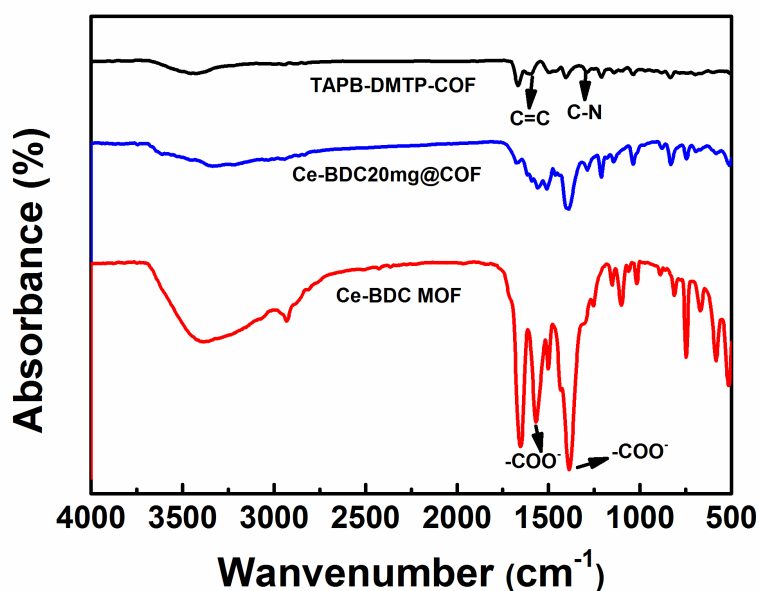

Figure 3. FTIR spectra of TAPB-DMTP-COF, Ce-BDC MOF, and the Ce-BDC@COF composite with an amount of 20 mg Ce-BDC MOF.

The XPS analysis was then executed to explore the surface chemical composition and electronic state of elements in a case of Ce-BDC@COF composite where the amount of Ce-BDC MOF is 20 mg. In its full survey XPS spectrum (**Figure 4a**), the presence of C, N, O, and Ce elements is confirmed. In its high-resolution XPS spectrum of C 1s (**Figure 4b**), the C–C peak appears at a binding energy of 284.6 eV, while the C–N and C=N peaks are seen at higher binding energies. In its high-resolution XPS spectrum of Ce (**Figure 4c**), Ce $3d_{5/2}$ and Ce $3d_{3/2}$ spin-orbit doublets are used to suit the Ce 3d spectrum. The peaks at 881.83 eV and 900.32 eV are corresponded to Ce^{4+}, while other fitted peaks at 885.84 eV and 903.88 eV are assigned to Ce^{3+} [45].
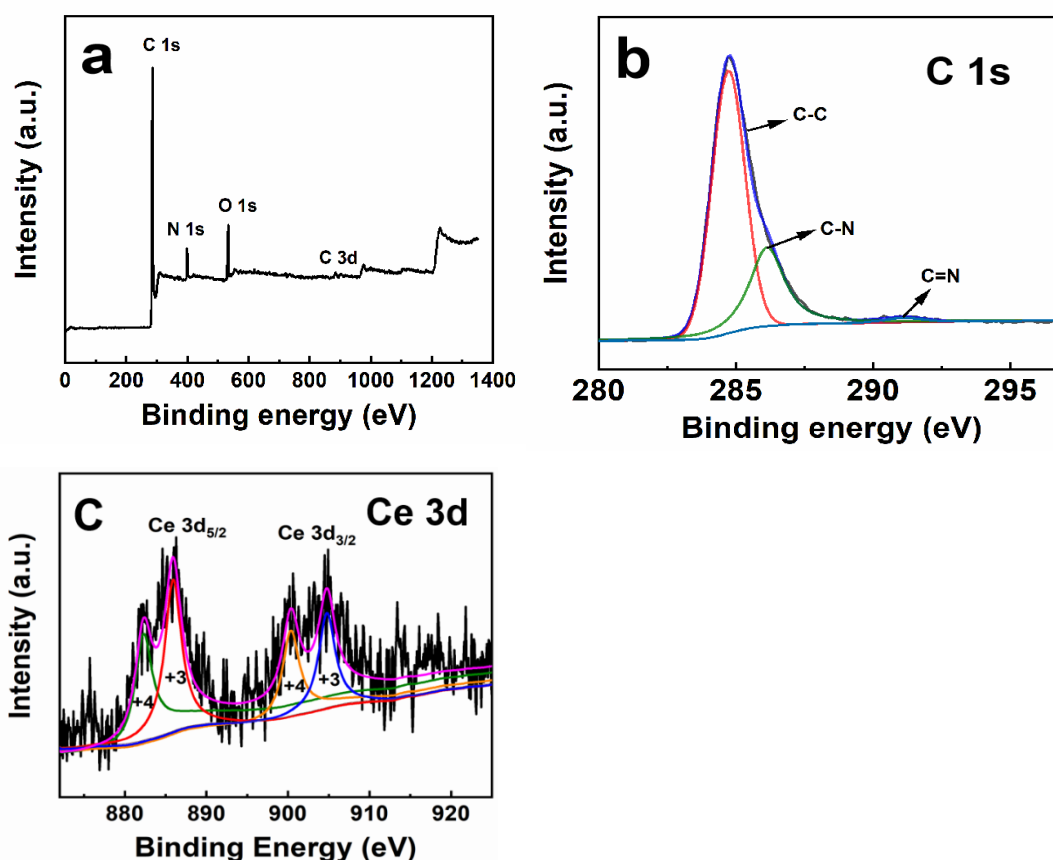
9

Figure 4. (a) XPS full survey of the Ce-BDC@COF composite with an amount of 20 mg Ce-BDC MOF, its high-resolution XPS spectra of C 1s (b) and (c) Ce 3d.

3.2 Electrochemical properties of Ce-BDC@COF composites

To explore the electrochemical properties of such composites different modified electrodes were fabricated using Ce-BDC MOF, TAPB-DMTP-COF, and a case Ce-BDC@COF composite with an amount of 20 mg Ce-BDC MOF. By means of cyclic voltammetry and electrochemical impedance spectroscopy, their cyclic voltammograms and Nyquist plots were recorded in a typical a $[Fe(CN)_6]^{3-/4-}$ redox probe solution. They are further compared with those on a GCE. In the cyclic voltammograms of a COF/GCE, a Ce-BDC/GCE, and a Ce-BDC@COF/GCE (**Figure 5a**), a pair of redox waves is clearly seen, similar to those of a GCE. The peak currents on the Ce-BDC@COF/GCE are higher than those on the GCE, while the peak currents on the COF/GCE are significantly smaller than those on the GCE. Under the same conditions, the peak currents follow a sequence of Ce-BDC@COF/GCE > Ce-BDC/GCE > GCE > COF/GCE. Therefore, the Ce-

10

BDC@COF perhaps has good conductivity and a large active area, while the COF severely inhibits the electron transfer of redox probes. Note that the peak currents on the Ce-BDC@COF/GCE are the highest, indicating that Ce-BDC probably improves the electron transfer ability of COF.

The Nyquist plots of these electrodes were utilized to get insight into their electron transfer rates, namely their charge-transfer resistances (R_{ct}). Based on the diameters of semi-circles in these Nyquist plots (**Figure 5b**), the R_{ct} values of the GCE, the COF/GCE, the Ce-BDC/GCE, and the Ce-BDC@COF/GCE are 71.1, 226.8, 58.4, and 17.85 Ω, respectively. Clearly, the Ce-BDC@COF/GCE possesses the fastest electron transfer rate among these electrodes, probably stemming from an excellent electrical conductivity of the Ce-BDC@COF composite, accelerated electron transport *via* the covalent bonds between MOF and COF, as well as an enlarged surface area.

The electroactive surface areas of these electrodes were then evaluated with the aid of the equation [46] of $I_P = (2.69 \times 10^5)n^{3/2}AD^{1/2}cv^{1/2}$, where v is the scan rate (V s^{-1}) that is applied to record related cyclic voltammograms, c is the concentration of the $[Fe(CN)_6]^{3-/4-}$ probe (M), D is the diffusion coefficient of $[Fe(CN)_6]^{3-/4-}$ (= 3.09×10^{-6} cm^2 s^{-1}), A is the electroactive area (cm^2), n (=1) is the number of transferred electrons, and I_P is the anodic or cathodic peak current (A). Based on the cyclic voltammograms of 5 mM $[Fe(CN)_6]^{3-/4-}$+ 0.10 M KCl on the GCE, the COF/GCE, the Ce-BDC/GCE, and the Ce-BDC@COF/GCE recorded at different scan rates (e.g., from 25 to 150 mV s^{-1}), the plots of the anodic peak currents (I_{pa}) were plotted as a function of the square roots of the scan rate ($v^{1/2}$). Using the slopes of these linear plots (**Figure 5c**), the calculated electroactive surface areas of a COF/GCE, a GCE, a Ce-BDC/GCE, and a Ce-BDC@COF/GCE are 0.092, 0.118, 0.141, and 0.149 cm^2 respectively. All these results confirm the excellent electrochemical performance of a Ce-BDC@COF/GCE.
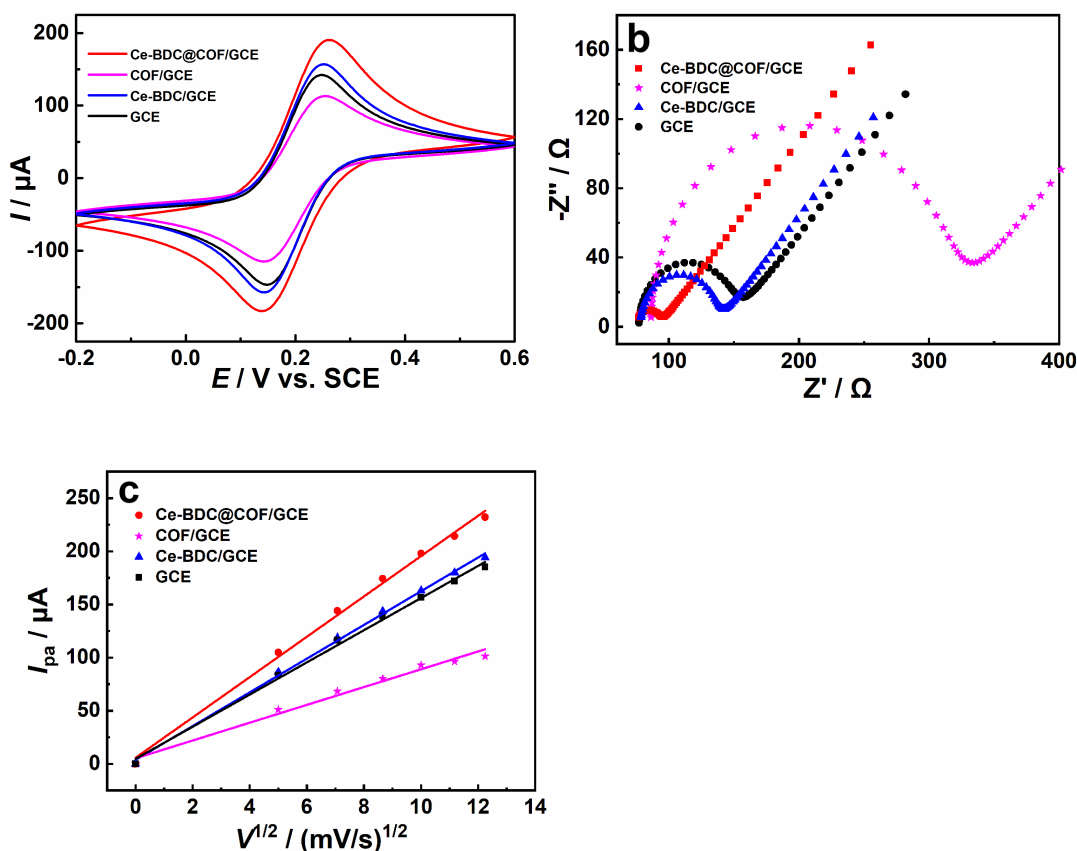
Figure 5. (a) Cyclic voltammograms of a GCE, a COF/GCE, a Ce-BDC/GCE, and a Ce-BDC@COF/GCE at a scan rate of 100 mV s^{-1} as well as (b) their Nyquist plots in 5 mM [Fe(CN)$_6$]$^{3-/4-}$ + 0.10 M KCl. (c) variation of oxidation peak currents with the square roots of scan rates.

3.3 Electrochemical applications *of Ce-BDC@COF composites*

Electrochemical applications of the Ce-BDC@COF/GCEs were further explored. As a case study, their electrochemical sensing of metol (p-methylaminophenol sulfate, **Figure S4**) was examined. The establishment of a simple and accurate method to detect metol is of great significance.

The cyclic voltammograms of 20 μM metol in 0.1 M pH 7.0 phosphorous buffer solution on different Ce-BDC@COF/GCEs were firstly recorded (**Figure S5**), where a pair of redox waves is seen on all electrodes, and the highest peak currents are obtained on the Ce-BDC@COF/GCE when the amount of Ce-BDC MOF is 20 mg. This demonstrates that an appropriate thickness of the TAPB-DMTP-COF in the Ce-BDC@COF composites is critical to achieving the best electrochemical response of

12

metol on the Ce-BDC@COF/GCE. For the following tests, the Ce-BDC@COF/GCE when the amount of Ce-BDC MOF of 20 mg (shorthand as Ce-BDC@COF/GCE) was selected.

To further reveal the enhanced electrochemical properties of this Ce-BDC@COF/GCE, the cyclic voltammograms of different modified GCEs were recorded in 20 μM metol in 0.1 M pH 7.0 phosphorous buffer solution at a scan rate of 100 mV s^{-1} (**Figure 6a**). As control experiments, the background currents of these electrodes were also recorded (**Figure 6b**), where no redox waves are seen within the scan potential range. Among these electrodes, the best electrochemical response, namely the highest peak currents and the smallest difference of peak potentials, is found on the Ce-BDC@COF/GCE. For example, the anodic peak current on the Ce-BDC@COF/GCE is as high as 1.78 μA, while that on a GCE is only 0.84 μA. The ratio of the anodic peak current (I_{pc}) to the cathodic one is 1.1, indicating that the electrode reaction of metol at this modified electrode is a (quasi-) reversible process. Further comparison of the response of metol on the Ce-BDC/GCE and the COF/GCE with that on the Ce-BDC@COF/GCE under the identified conditions, one can find an obvious synergistic effect between Ce-BDC MOF and the TAPB-DMTP-COF toward the voltammetric sensing of metol. The potential ways are assumed as follows. First, a porous COF has a fascinating 2D structure or a large specific area, leading to an increased electro-active surface area; Second, the porous Ce-BDC is possible to improve the oxidation process of metol; Third, COF is one organic polymer and endows π-π bonds. The metol has benzene rings. Through the interaction of π-π stacking between COF and metol, the adsorption of metol on the Ce-BDC@COF/GCE is possible to be enhanced.
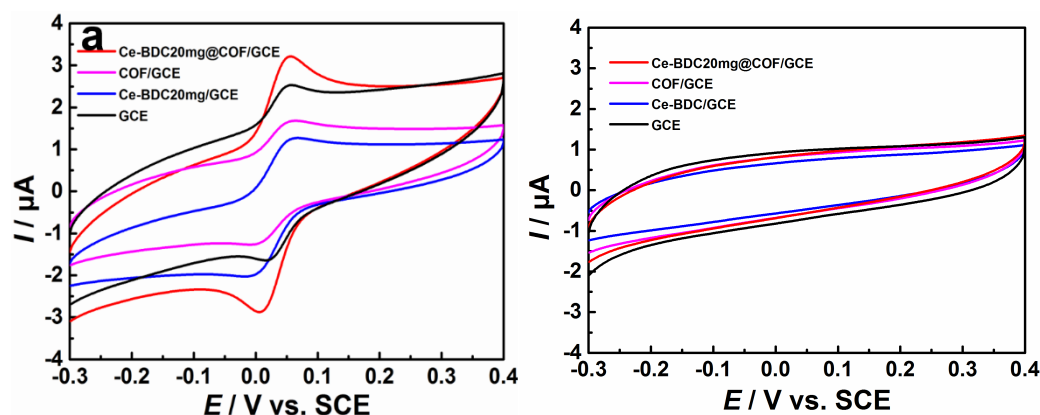

Figure 6. Cyclic voltammograms in the presence (a) and absence of 20 μM metol in

13

0.1 M pH 7.0 phosphate buffer solution at a scan rate of 100 mV s^{-1} on a GCE, a COF/GCE, a Ce-BDC/GCE, and a Ce-BDC@COF/GCE.

Electrode kinetic of metol on a Ce-BDC@COF/GCE was further investigated by recording the cyclic voltammograms of 20 μM in 0.1 M pH 7.0 phosphate buffer solution at different scan rates (**Figure S6a**), where a pair of redox wave is clearly seen. Moreover, the anodic peak current (I_{pa}) is linearly increased as a function of the square root of the scan rate (**Figure S6b**), indicating a diffusion-control redox process of metol on this modified electrode. Furthermore, the anodic peak potential (E_{pa}) is linearly varied as a function of the natural logarithm of scan rate (lnυ) (**Figure S6b**). With aid of the Laviron's equation and the slope between E_{pa} and lnυ, the number of electrons transferred during the redox reaction of metol at the Ce-BDC@COF/GCE is two.

The cyclic voltammograms of 20 μM on a Ce-BDC@COF/GCE in 0.1 M phosphate buffer solution with different pH values were also recorded (**Figure S7a**), where a pair of redox wave is clearly seen. When the pH value of 0.1 M phosphate buffer solution is changed from 6.0 to 7.0, the I_{pa} value is gradually enhanced, which is then inversely reduced when the pH value is higher than 7.0 (**Figure S7b**). Therefore, 0.1 M pH 7.0 phosphate buffer solution was chosen for all related electrochemical tests. Moreover, the E_{pa} value linearly shifts towards the negative potential with an increase in pH value of 0.1 M phosphate buffer solution (**Figure S7c**). According to the slope of the linearity between E_{pa} and the pH value of 0.1 M phosphate buffer solution (= 59 mV pH^{-1}), the equal number of proton and electron is confirmed. Namely, the number of involved protons is also two during the redox reaction of metol at the Ce-BDC@COF/GCE. In short, the redox reaction of metol on the Ce-BDC@COF/GCE is a (quasi-) reversible, diffusion-controlled, two protons/electrons involved electrode process.

Sensitive detection of metol on the Ce-BDC@COF/GCE was then conducted by means of differential pulse voltammetry. Prior to it, the detection conditions were optimized, including the used volume of the Ce-BDC@COF suspension as well as accumulation potential and time. An increase in the volume of the Ce-BDC MOF@COF suspension leads to the enhancement of the I_{pa} value and then its reduction. When the volume is 5.0 μL, the highest I_{pa} value is obtained (**Figure S8a**).

14

This is perhaps because an excessive amount of Ce-BDC MOF@COF on the GCE surface slows down the electron transfer rate of metol. As for accumulation potential, the I_{pa} value is increased when it is increased from -0.5 to -0.1 V and then decreased (**Figure S8b**). With respect to accumulation time, the highest I_{pa} value is obtained when it is 60 s. A shorter or longer accumulation time leads to a smaller I_{pa} value (**Figure S8c**). Therefore, a volume of Ce-BDC MOF@COF suspension of 5.0 μL, an accumulation potential of t -0.1 V, and an accumulation time of 60 s were chosen for the metol detection on the Ce-BDC@COF/GCE.

Under these optimal conditions, the differential pulse voltammograms of metol at different concentrations in 0.1 M pH 7.0 phosphate buffer solution were recorded at a scan rate of 100 mV s^{-1} (**Figure 7a**), where the I_{pa} value is varied as a function of the metol concentration. The linear relationship is observed between the I_{pa} value and the metol concentration (C) over the range of 0.1 to 200 μM (**Figure 7b**), following a linear equation of $I_p = 0.1142C + 0.00212$ ($R^2 = 0.996$). The calculated detection limit is 30 nM. Compared with the metol sensors reported in recent years, this sensor shows a comparable detection limit and wide linear range, indicating its wonderful application prospect (**Table 1**).
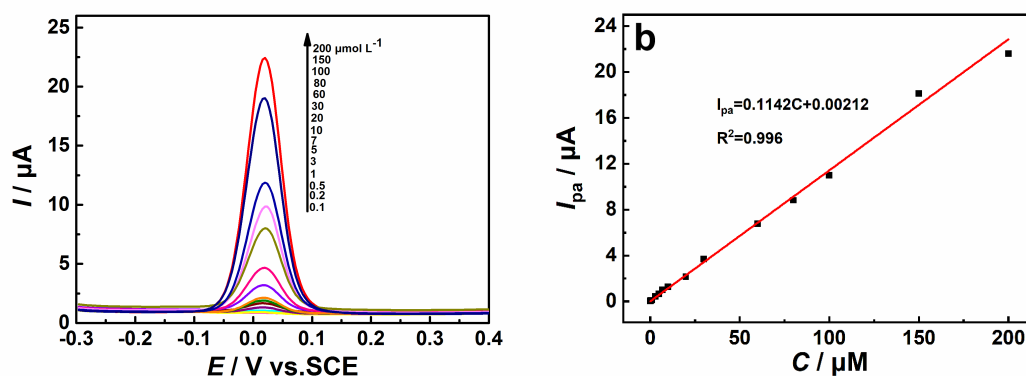

Figure 7. (a) Differential pulse voltammograms of metol with different concentrations in 0.1 M pH 7.0 phosphate buffer solution at a scan rate of 100 mV s^{-1}; (b) the variation of the I_{pa} values as a function of the metol concentration.

Table 1. Comparison of MOF@COF modified electrode with other reported materials in metol detection

Modified electrode	linear range (μM)	detection limit (nM)	ref

15

CoMn$_2$O$_4$@RGO[a]	0.01–137.65	50	[47]
MoS$_2$	0.2–1211	10	[48]
GO@CoMoSe$_2$	0.04–123	9.0	[49]
Cu$_2$Co$_2$O$_4$	0.02–10000	6.0	[50]
LiCoO$_2$/CILE[b]	0.4–400	24.6	[51]
GO/CeNbO$_4$	0.02-356	10	[52]
MOF@COF	0.1 -200	30	This work

[a]RGO=reduced graphene oxide; [b]CILE= carbon ionic liquid electrode

The repeatability, reproducibility and stability of the metol detection on the Ce-BDC@COF/GCE were further tested. The repeatability tests were conducted by successive determination of 5 μM metol in 0.1 M pH 7.0 phosphate buffer solution for 6 times. The obtained relative standard deviation (RSD) was 1.6 %. The reproducibility tests were carried out by comparing the detection signals of 5 μM metol in 0.1 M pH 7.0 phosphate buffer solution on 6 Ce-BDC@COF/GCEs. Other conditions were the same. The calculated RSD was 3.5%. The stability tests were done by measuring 5 μM metol in 0.1 M pH 7.0 phosphate buffer solution 7 times over 21 days on the same Ce-BDC@COF/GCE. After 21 days, the I_{pa} value was kept at 78% of its initial value.

The selectivity of the Ce-BDC@COF/GCE towards the metol detection was also examined. For such a purpose, various foreign species were added into 5 μM metol in 0.1 M pH 7.0 phosphate buffer solution. The level of tolerance for the added species was defined by percentage in the I_{pa} value of metol. The addition of 40-folds K$^+$/Ca^{2+}/Al^{3+}/Cl$^-$/SO$_4^{2-}$, 10-folds 2,4-DCP/TCS, and 4-folds BPA/HQ/CC/RC have almost no interference on the determination of metol on the Ce-BDC@COF/GCE (**Figure S9**), confirming its high selectivity for the metol detection. Consequently, the Ce-BDC@COF/GCE possesses excellent repeatability, reproducibility, stability, and selectivity toward the metol detection.

The Ce-BDC@COF/GCE was finally employed to detect metol in the real samples. Supermarket receipts and lake water were selected as real samples to evaluate the practicability of the proposed sensor. For supermarket receipts, 100 μL of pre-treated filtrate was added into 10 mL of 0.1 M pH 7.0 phosphate buffer solution to measure its metol content. While the lake water sample was diluted twice with 0.2 M pH 7.0

phosphate buffer solution to monitor the metol. The results are summarized in Table S1. Through a standard addition method, the recoveries of these measurements are in the range of 102.0% – 106.0% and 108.0% – 115.7%, giving RSD values of 1.1% – 3.2% and 0.3% to-3.8% for supermarket receipt and lake water respectively. Therefore, this Ce-BDC@COF/GCE is sensitive and selective enough for metol detection in real samples.

4. Conclusion

In summary, a novel core-shell MOF@COF composite has been prepared. Thanks to the unique features of both MOFs and COFs, such a composite possesses a big active surface area and fast electrode kinetic toward electroactive species in solutions, including redox probes and metol – a case target to explore electrochemical applications of this core-shell MOF@COF composite. As for the metol detection, these composite modified electrodes exhibited a wide detection range, a low detection limit, high reproducibility/repeatability/sensitivity, as well as excellent selectivity. Such improved performance is assumed to stem from the synergistic effect of the interlayer π-π electron clouds of COFs and the unique properties of MOFs. Such composites thus promote electrochemical applications of COFs (e.g., sensing, emery storage) and can be further applied for photocatalysis, gas adsorption, and separation.

Appendix A. Supplementary data

Supplementary data to this article can be found online at

References

[1] T. Ni, D. Zhang, J. Wang, S. Wang, H. Liu, B. Sun, Grafting of quantum dots on covalent organic frameworks via a reverse microemulsion for highly selective and sensitive protein optosensing, Sens. Actuators, B 269 (2018) 340-345.
[2] K. Geng, T. He, R. Liu, S. Dalapati, K.T. Tan, Z. Li, S. Tao, Y. Gong, Q. Jiang, D. Jiang, Covalent organic frameworks: design, synthesis, and functions, Chem. Rev. 120(16) (2020)

8814-8933.

[3] M.S. Lohse, T. Bein, Covalent organic frameworks: structures, synthesis, and applications, Adv. Funct. Mater. 28(33) (2018).

[4] J. Yang, L.J. Huang, J.M. You, Y. Yamauchi, Magnetic covalent organic framework composites for wastewater remediation, Small (2023) 2301044.

[5] L.J. Huang, J. Yang, Y.J. Zhao, H. Miyata, M.S. Han, Q. Shuai, Y. Yamauchi, Monolithic covalent organic frameworks with hierarchical architecture: attractive platform for contaminant remediation, Chem. Mater. (2023) 2661-2682.

[6] T. Zhang, C. Gao, W. Huang, Y. Chen, Y. Wang, J. Wang, Covalent organic framework as a novel electrochemical platform for highly sensitive and stable detection of lead, Talanta 188 (2018) 578-583.

[7] A.P. Cote, A.I. Benin, N.W. Ockwig, M. O'Keeffe, A.J. Matzger, O.M. Yaghi, Porous, crystalline, covalent organic frameworks, Science 310(5751) (2005) 1166-1170.

[8] O. Buyukcakir, S.H. Je, S.N. Talapaneni, D. Kim, A. Coskun, Charged covalent triazine frameworks for CO_2 capture and conversion, ACS applied materials & interfaces 9(8) (2017) 7209-7216.

[9] X. Hang, J. Huang, C. Yuan, Y. Liu, Y. Cui, Chiral 3D covalent organic frameworks for high performance liquid chromatographic enantioseparation, J. Am. Chem. Soc. 140(3) (2018) 892-895.

[10] D. Kong, T. Bao, Z. Chen, In situ synthesis of the imine-based covalent organic framework LZU1 on the inner walls of capillaries for electrochromatographic separation of nonsteroidal drugs and amino acids, Microchim. Acta 184(4) (2017) 1169-1176.

[11] H. Xu, J. Gao, D. Jiang, Stable, crystalline, porous, covalent organic frameworks as a platform for chiral organocatalysts, Nat. Chem. 7(11) (2015) 905-912.

[12] P. Bhanja, K. Bhunia, S.K. Das, D. Pradhan, R. Kimura, Y. Hijikata, S. Irle, A. Bhaumik, new triazine-based covalent organic framework for high-performance capacitive energy storage, ChemSusChem 10(5) (2017) 921-929.

[13] X.-C. Li, Y. Zhang, C.-Y. Wang, Y. Wan, W.-Y. Lai, H. Pang, W. Huang, Redox-active triazatruxene-based conjugated microporous polymers for high-performance supercapacitors, Chem. Sci. 8(4) (2017) 2959-2965.

[14] Q. Fang, J. Wang, S. Gu, R.B. Kaspar, Z. Zhuang, J. Zheng, H. Guo, S. Qiu, Y. Yan, 3D porous crystalline polyimide covalent organic frameworks for drug delivery, J. Am. Chem. Soc. 137(26) (2015) 8352-8355.

[15] W. Wang, W. Zhao, H. Xu, S. Liu, W. Huang, Q. Zhao, Fabrication of ultra-thin 2D covalent organic framework nanosheets and their application in functional electronic devices, Coord. Chem. Rev. 429 (2021) 213616 .

[16] Q. Guan, L.-L. Zhou, W.-Y. Li, Y.-A. Li, Y.-B. Dong, Covalent organic frameworks (COFs) for cancer therapeutics, Chem. Euro. J. 26(25) (2020) 5583-5591.

[17] W. Ma, Q. Zheng, Y. He, G. Li, W. Guo, Z. Lin, L. Zhang, Size-controllable synthesis of uniform spherical covalent organic frameworks at room temperature for highly efficient and selective enrichment of hydrophobic peptides, J. Am. Chem. Soc. 141(45) (2019) 18271-18277.

[18] H. Liao, H. Ding, B. Li, X. Ai, C. Wang, Covalent-Organic Frameworks: potential host materials for sulfur impregnation in lithium-sulfur batteries, J. Mater. Chem. A 2(23) (2014) 8854-8858.

[19] P. Ramakrishnan, S. Shanmugam, Nitrogen-doped porous multi-nano-channel nanocarbons for use in high-performance supercapacitor applications, ACS Sustainable Chem. Eng. 4(4) (2016) 2439-2448.

[20] L.-F. Chen, Q. Xu, Converting MOFs into amination catalysts, Science 358(6361) (2017) 304-305.

[21] Y.-B. Huang, J. Liang, X.-S. Wang, R. Cao, Multifunctional metal-organic framework catalysts: synergistic catalysis and tandem reactions, Chem. Soc. Rev. 46(1) (2017) 126-157.

[22] A. Bavykina, N. Kolobov, I.S. Khan, J.A. Bau, A. Ramirez, J. Gascon, Metal-organic frameworks in heterogeneous catalysis: recent progress, new trends, and future perspectives, Chem. Rev. 120(16) (2020) 8468-8535.

[23] T. Qiu, Z. Liang, W. Guo, H. Tabassum, S. Gao, R. Zou, Metal-organic framework-based

materials for energy conversion and storage, ACS Energy Lett. 5(2) (2020) 520-532.

[24] X. Feng, Y. Pi, Y. Song, C. Brzezinski, Z. Xu, Z. Li, W. Lin, Metal-organic frameworks significantly enhance photocatalytic hydrogen evolution and CO_2 reduction with earth-abundant copper photosensitizers, J. Am. Chem. Soc. 142(2) (2020) 690-695.

[25] G.S. Yuan, L.C. Tan, P. Wang, Y.C. Wang, C.J. Wang, H.J. Yan, Y.Y. Wang, MOF-COF composite photocatalysts: design, synthesis, mechanism, Crystal Growth & Design 22(1) (2022) 893-908.

[26] Z.L. Wu, W. Li, L.L. Hou, Q.M. Wei, H.X. Yang, Y.Y. Jiang, D.Y. Tang, A novel sunflower-like MOF@COF for improved photocatalytic CO_2 reduction, Sep. Purif. Technol. 311 (2023) 123322.

[27] C. Zhang, B.H. Wu, M.Q. Ma, Z.K. Wang, Z.K. Xu, Ultrathin metal/covalent-organic framework membranes towards ultimate separation, Chem. Soc. Rev. 48(14) (2019) 3811-3841.

[28] S. Aydin, C. Altintas, I. Erucar, S. Keskin, Computational investigation of dual filler-incorporated polymer membranes for efficient CO_2 and H_2 separation: MOF/COF/Polymer mixed matrix membranes, Ind. Eng. Chem. Res. 62(6) (2023) 2924-2936.

[29] J.R. Fu, S. Das, G.L. Xing, T. Ben, V. Valtchev, S.L. Qiu, Fabrication of COF-MOF composite membranes and their highly selective separation of H_2/CO_2, J. Am. Chem. Soc. 138(24) (2016) 7673-7680.

[30] H.W. Zhang, Q.Q. Zhu, R.R. Yuan, H.M. He, Crystal engineering of MOF@COF core-shell composites for ultra-sensitively electrochemical detection, Sens. Actuators, B 329 (2021) 129144 .

[31] X.K. Liu, M.Y. Hu, M.H. Wang, Y.P. Song, N. Zhou, L.H. He, Z.H. Zhang, Novel nanoarchitecture of Co-MOF-on-TPN-COF hybrid: ultralowly sensitive bioplatform of electrochemical aptasensor toward ampicillin, Biosens. Bioelectron. 123 (2019) 59-68.

[32] N. Zhou, Y.S. Ma, B. Hu, L.H. He, S.J. Wang, Z.H. Zhang, S.Y. Lu, Construction of Ce-MOF@COF hybrid nanostructure: Label-free aptasensor for the ultrasensitive detection of oxytetracycline residues in aqueous solution environments, Biosens. Bioelectron. 127 (2019) 92-100.

[33] Y. Peng, M. Zhao, B. Chen, Z. Zhang, Y. Huang, F. Dai, Z. Lai, X. Cui, C. Tan, H. Zhang, Hybridization of MOFs and COFs: a new strategy for construction of MOF@COF core-shell hybrid materials, Adv. Mater. 30(3) (2018) 1705454.

[34] F.-M. Zhang, J.-L. Sheng, Z.-D. Yang, X.-J. Sun, H.-L. Tang, M. Lu, H. Dong, F.-C. Shen, J. Liu, Y.-Q. Lan, Rational design of MOF/COF hybrid materials for photocatalytic H_2 evolution in the presence of sacrificial electron donors, Angew. Chem., Int. Ed. 57(37) (2018) 12106-12110.

[35] R. Andreozzi, V. Caprio, A. Insola, R. Marotta, The oxidation of metol (N-methyl-p-aminophenol) in aqueous solution by UV/H_2O_2 photolysis, Water Res. 34(2) (2000) 463-472.

[36] L. Lunar, D. Sicilia, S. Rubio, D. Pérez-Bendito, U. Nickel, Identification of metol degradation products under Fenton's reagent treatment using liquid chromatography-mass spectrometry, Water Res. 34(13) (2000) 3400-3412.

[37] C.D. Stalikas, L. Lunar, S. Rubio, D. Pérez-Bendito, Degradation of medical X-ray film developing wastewaters by advanced oxidation processes, Water Res. 35(16) (2001) 3845-3856.

[38] P. Zhao, F. Qin, Z. Huang, C. Sun, W. Shen, H. Xu, MOF-derived hollow porous Ni/CeO_2 octahedron with high efficiency for N_2O decomposition, Chem. Eng. J. 349 (2018) 72-81.

[39] X. Shi, Y. Yao, Y. Xu, K. Liu, G. Zhu, L. Chi, G. Lu, Imparting catalytic activity to a covalent organic framework material by nanoparticle encapsulation, ACS Appl. Mater. Interfaces 9(8) (2017) 7481-7488.

[40] M. Lammert, M.T. Wharmby, S. Smolders, B. Bueken, A. Lieb, K.A. Lomachenko, D. De Vos, N. Stock, Cerium-based metal organic frameworks with UiO-66 architecture: synthesis, properties and redox catalytic activity, Chem. Commun. 51(63) (2015) 12578-12581.

[41] J. Yang, C. Zheng, P. Xiong, Y. Li, M. Wei, Zn-doped Ni-MOF material with a high supercapacitive performance, J. Mater. Chem. A 2(44) (2014) 19005-19010.

[42] G.-C. Li, P.-F. Liu, R. Liu, M. Liu, K. Tao, S.-R. Zhu, M.-K. Wu, F.-Y. Yi, L. Han, MOF-derived hierarchical double-shelled NiO/ZnO hollow spheres for high-performance

supercapacitors, Dalton Trans. 45(34) (2016) 13311-13316.

[43] G. Zeng, Y. Chen, L. Chen, P. Xiong, M. Wei, Hierarchical cerium oxide derived from metal-organic frameworks for high performance supercapacitor electrodes, Electrochim. Acta 222 (2016) 773-780.

[44] F. Zhang, L. Hao, L. Zhang, X. Zhang, Solid-state thermolysis preparation of Co_3O_4 nano/micro superstructures from metal-organic framework for supercapacitors, Int. J. Electrochem. Sci. 6(7) (2011) 2943-2954.

[45] P. Zhang, Z.Q. Ding, X.Y. Liu, Y. Chen, X.R. Zeng, C.Q. Tang, In-situ synthesis of magnetic Ce-BDC@Fe_3O_4 metal-organic frameworks and their multiple enzyme-mimicking catalysis, Micro Nano Lett. 17(9) (2022) 201-209.

[46] S. Shahrokhian, L. Naderi, M. Ghalkhani, Modified glassy carbon electrodes based on carbon nanostructures for ultrasensitive electrochemical determination of furazolidone, Mater. Sci. Eng., C 61 (2016) 842-850.

[47] K. Venkatesh, B. Muthukutty, S.M. Chen, P. Karuppasamy, A.S. Haidyrah, C. Karuppiah, C.C. Yang, S.K. Ramaraj, Spinel $CoMn_2O_4$ nano-/micro-spheres embedded RGO nanosheets modified disposable electrode for the highly sensitive electrochemical detection of metol, J. Ind. Eng. Chem. 106 (2022) 287-296.

[48] C. Koventhan, V. Vinothkumar, S.M. Chen, T.W. Chen, A. Sangili, K. Pandi, V. Sethupathi, Efficient hydrothermal synthesis of flake-like molybdenum disulfide for selective electrochemical detection of metol in water real samples, Int. J. Electrochem. Sci. 15(8) (2020) 7390-7406.

[49] S. Ramaraj, M. Sakthivel, S.M. Chen, K.C. Ho, Correction to active-site-rich 1T-phase $CoMoSe_2$ integrated graphene oxide nanocomposite as an efficient electrocatalyst for electrochemical sensor and energy storage applications, Anal. Chem. 92(2) (2020) 2347-2348.

[50] S. Samanta, R. Srivastava, $CuCo_2O_4$ based economical electrochemical sensor for the nanomolar detection of hydrazine and metol, J. Electroanal. Chem. 777 (2016) 48-57.

[51] W. Sun, Y. Deng, J. Liu, W. Liu, Y. Cheng, L. Wang, Y. Gu, Electrochemical behavior and voltammetric determination of p-methylaminophenol sulfate using $LiCoO_2$ nanosphere modified electrode, Thin Solid Films 564 (2014) 379-383.

[52] B. Mutharani, P.K. Gopi, S.M. Chen, H.C. Tsai, F. Ahmed, A.S. Haidyrah, P. Ranganathan, Amperometric determination of ecotoxic N-methyl-p-aminophenol sulfate in photographic solution and river water samples based on graphene oxide/$CeNbO_4$ nanocomposite catalyst, Ecotoxicol. Environ. Saf. 220 (2021) 112373.